PURPOSE-LED
PUBLISHING™

PAPER • OPEN ACCESS

Transportation behaviour of OH and H_2O_2 in plasma-treated water

View the article online for updates and enhancements.

Transportation behaviour of OH and H$_2$O$_2$ in plasma-treated water

Hanna-Friederike Poggemann[1,8] ⬛, **Steffen Schüttler**[2,8] ⬛, **Anna Lena Schöne**[3,4,8] ⬛, **Emanuel Jeß**[2] ⬛, **Lars Schücke**[3,4] ⬛, **Timo Jacob**[1,5,7], **Andrew R Gibson**[3,6] ⬛, **Judith Golda**[2] ⬛ and **Christoph Jung**[1,5,7,*] ⬛

[1] Institute of Electrochemistry, Ulm University, Ulm, Germany
[2] Plasma Interface Physics, Ruhr University Bochum, Bochum, Germany
[3] Research Group for Biomedical Plasma Technology, Ruhr University Bochum, Bochum, Germany
[4] Chair of Applied Electrodynamics and Plasma Technology, Ruhr University Bochum, Bochum, Germany
[5] Helmholtz Institute Ulm (HIU) Electrochemical Energy Storage, Ulm, Germany
[6] York Plasma Institute, School of Physics, Engineering and Technology, University of York, York, United Kingdom
[7] Karlsruhe Institute of Technology (KIT), Karlsruhe, Germany

E-mail: christoph.jung@kit.edu

CrossMark

Abstract

The transportation of plasma-generated species through a liquid environment is a key step within the plasma-driven biocatalysis process, but is also of great importance for other systems with plasma–liquid interfaces. The aim of this study is to explore the transportation processes and lifetime of plasma-generated species in an aqueous solution. Therefore, a combination of experimental methods, reactive molecular dynamics (MD) simulations, and reaction–diffusion modelling was used. Experimentally, an atmospheric pressure plasma jet was used to treat an aqueous sample. Convective transport was visualized by particle image velocimetry in the plasma-treated water. Chemiluminescence measurements of OH were conducted by the use of luminol and 2D-UV-absorption spectroscopy was used to detect H$_2$O$_2$ in the plasma-treated water. The strength of convective transport was found to decrease with the gas flow rate through the jet, and at low gas flows, an effective diffusion coefficient for H$_2$O$_2$ could be calculated. OH was mainly present at the liquid surface under all treatments investigated. The reactive MD simulations form the basic model of an ideal system, where all transportation is purely diffusion-driven, and molecular diffusion coefficients can be calculated. The results of the MD simulations were compared with the experimental studies to gain a deeper understanding of the differences between the ideal and the real system. To bridge the gap between the time scales of the MD simulations and the experiments, a kinetic model was used to understand the spatio-temporal changes and the influence of transport mechanisms and reaction chemistry. For low flow rate cases good agreement between experimental measurements and kinetic modelling could be obtained when the experimentally measured effective diffusion coefficient was used as

[8] Authors contributed equally to this work.
[*] Author to whom any correspondence should be addressed.

input to the model. The differences in the H_2O_2 concentration profiles in the liquid when using the molecular diffusion coefficient derived from MD and the effective diffusion coefficient from the experimental measurements are highlighted.

Supplementary material for this article is available online

1. Introduction

In recent years low-temperature atmospheric pressure plasmas gained importance in several fields, from biomedical to catalytic applications [1–4]. Often, the interaction between plasmas and liquids is important, especially in biological applications [5, 6]. However, we are still lacking detailed knowledge about the chemical behaviour of plasma species in liquid environments. Depending on the specific application of the plasma-treated liquid, understanding the stability parameters and transportation processes is crucial.

Dickenson and colleagues stated in their publication that there are two important requirements when choosing the plasma source for a specific application: the operating conditions of the plasma source should favour the generation of the desired reactive species and the amount of reactive species should be adequate for the surface area of the target [7]. Our study investigates plasma-treated liquids in the context of plasma-assisted biocatalysis, an innovative approach that attempts to solve the supply problems of biocatalysis by using plasma-generated species as reactants for the catalytic reaction [8–10]. In our experimental setup, a capillary plasma jet is used, because it fits the targets of species production and their delivery to liquid environments, and allows the fine-tuning of the species production. The transportation of the plasma species through the gas phase to the liquid surface has already been studied by our group [11], now we want to build on these findings and take a closer look at the transportation in the liquid. The study is focused on H_2O_2 and OH because certain enzymes utilize H_2O_2 [8, 10], and OH is the most important precursor in the production of H_2O_2 by atmospheric pressure plasmas [11–14].

However, using a plasma jet for in-line production is challenging because the reactive plasma species can alter and deactivate the enzymes used in biocatalysis. Thus, the research focus lies on transportation mechanisms through the treated liquid, as well as the stability of the species. Several groups have started to investigate this process and the resulting phenomena over the past years by experimental works [15–17] and modelling approaches [18–22]. Although it is often challenging to compare experiments and simulations, both show similar phenomena. The effluent of plasma jets impinging on a liquid surface shows the formation of vortices on the liquid surface, inducing convective transport of species diluted in the liquid. Furthermore, diffusion of the species in the liquid is also present, due to the concentration gradient of diluted species in the liquid.

To extend this research, a combination of experimental studies, molecular dynamics (MD) simulations, and kinetic modelling were performed to bridge the gap between theoretical chemistry and experimental physics. Combining these methods enables the comparison between the behaviour on short time scales, in the range of 1 ns, and effects taking place in the range of several minutes. For the molecular dynamic simulations, the reactive MD framework ReaxFF was chosen, first developed by van Duin *et al* [23], to gain insights into the diffusive behaviour as well as the chemical reactions of the plasma generated species with the surrounding liquid. All our studies were performed at room temperature since that fits the *modus operandi* of the plasma-driven biocatalysis. The experiments were conducted using an atmospheric pressure plasma jet operated in humid He, treating an aqueous liquid sample. 2D UV absorption spectroscopy was used to detect H_2O_2 in the liquid and visualize its distribution. Luminol was added to the liquid to visualize the distribution of OH by chemiluminescence (CL), and particle image velocimetry (PIV) was used to visualize and quantify the convective transport in the plasma-treated liquid. Further, kinetic modelling connects the experiments and the molecular dynamic simulations by solving the reaction–diffusion equation for OH and H_2O_2 over time and length scales that bridge the gap between those accessible in MD simulations and the experiment.

Our goal is to build a diffusion and transport model for plasma-generated species in a liquid environment that can prove useful for our specific application, as well as other research fields working with plasma-treated liquids. The paper is structured as follows. First, the experimental setup and the liquid diagnostics are explained. Then the calculation details of MD simulation and kinetic modelling are described. The results and discussion begin with the experimental part, followed by the MD simulation and the kinetic modelling that links the experiments and the MD simulation. Finally, the results are summarized.

2. Plasma experiments

2.1. Plasma jet and liquid treatment

The plasma jet used was a capillary plasma jet operated at 13.56 MHz excitation frequency in He feed gas. It was first
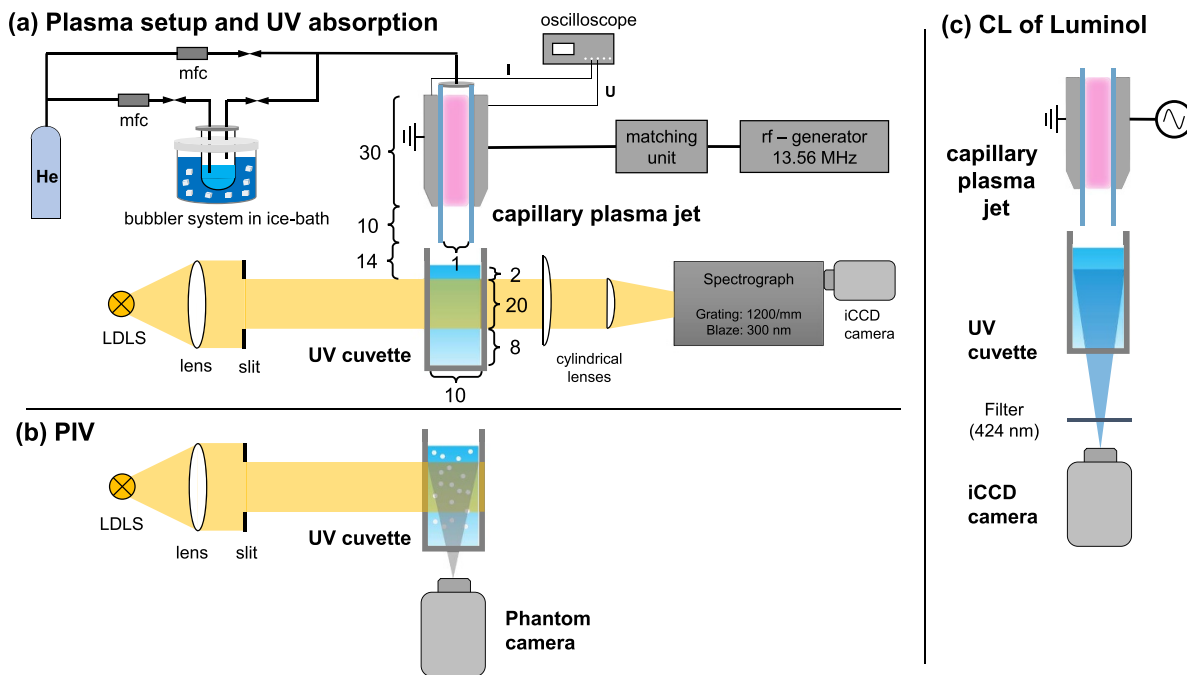
Figure 1. Setup of plasma experiments. (a) Plasma jet with gas and power supply as well as setup of the UV absorption spectroscopy. Dimensions are given in mm. (b) Setup of particle image velocimetry (PIV). (c) Setup to detect the chemiluminescence of luminol.

investigated by Winzer *et al* [24] and was previously used for treating liquids [25]. The capillary plasma jet is a further development of the well-investigated COST reference plasma jet [26] and consists of two 1 mm wide and 40 mm long stainless steel electrodes, one grounded and one powered. Between the two electrodes, a borosilicate capillary (CM Scientific) is placed. The capillary used had an inner cross-section of 1 mm^2 and a wall thickness of 0.2 mm to cover the total gap between the electrodes and their length. Thus, the plasma volume was 40 mm^3 and the electrode gap was 1.4 mm.

A schematic overview of power and gas supplies is shown in figure 1(a). The power was coupled via a matchbox (Coaxial Power Systems MMN 150) to minimize reflected power and was delivered by an RF generator (Coaxial Power Systems RFG 150). Power measurements were performed as described in [27] and a detailed description can be found there. In brief, the dissipated plasma power was calculated by $P = U \cdot I \cdot \cos \Phi$ with the voltage U, the current I, and the phase shift Φ between voltage and current. An oscilloscope (Teledyne LeCroy HDO6104A, $10\,\mathrm{GS\,s^{-1}}$) was used for measuring the voltage and current waveforms. A miniaturised voltage probe mounted in parallel behind the powered electrode was used to measure the voltage. Calibration with a commercial high-voltage probe (Tektronix P5100A) resulted in calibration factors between 100 and 200. Using Ohm's law, the current was measured across a $4.7\,\Omega$ resistor positioned between the grounded electrode and ground.

The gas flow was controlled by mass flow controllers (Analyt-MTC). One part of the He feed gas was guided through an ice-cooled bubbler at a temperature of $T = 1.4 \pm 0.5\,°\mathrm{C}$, to add water vapour to the gas flow. Two humidity admixtures were used by passing 10% or 100% of the gas flow

through the bubbler, resulting in humidity concentrations of (640 ± 30) ppm and (6400 ± 250) ppm, respectively.

For liquid treatments, 3 ml of solutions were filled into UV-cuvettes (Sarstedt polystyrene) using micro pipettes (Eppendorf). The plasma jet was adjusted to the desired plasma parameters (gas flow and plasma power) and lowered so that the capillary end was at the edge of the cuvette. In this way, the distance between the plasma and the liquid surface was 24 mm, with 10 mm of the effluent flowing through the capillary after it left the active plasma zone. Thereby, the effluent was protected from the ambient air for 10 mm, while mixing with the ambient air the rest of the way. Evaporation was measured for a gas flow rate of 1 slm to be less than 4%.

2.2. H_2O_2 detection: UV absorption

H_2O_2 absorbs light in the UV range from 180 nm to 300 nm [28, 29], which can be used to detect its concentration in plasma-treated liquids [30–33]. In this work, broadband emission (190–2500 nm) from a laser-driven light source (Energetiq EQ99X-FC) was passed through a UV lens and a slit, into a cuvette (width of 10 mm) filled with 3 ml distilled water. The light beam passed through the centre of the cuvette and had a width of 5 mm to avoid reflections at the sides. The height of the light beam was 20 mm and started 2 mm beneath the liquid surface, to not be disturbed by interactions at the liquid surface. After passing through the cuvette, cylindrical lenses (100 mm focal length) were used to shrink the light beam to the dimensions of the entrance slit (2 mm × 10 mm) of an imaging spectrometer, without loss of spatial resolution. The spectrometer (Acton Research Corporation 300i,

J. Phys. D: Appl. Phys. **58** (2025) 135208

H-F Poggemann *et al*

0.3 m focal length) was equipped with a 1200 lines/mm grating at blaze wavelength of 300 nm and the central wavelength was set to 250 nm. Calibration of the wavelength was performed by a Ne-Penray lamp (LOT-Oriel LSP032), resulting in an observable wavelength range from 237 nm to 271 nm. An intensified charge-coupled device (iCCD) camera (Andor iStar) was used to monitor the spectrum. The camera was operated with a gain of 10 and an exposure time of 40 ms. Kinetic series were captured with cycle times and number of images of 0.25 s and 1250 images or 1 s and 1800 images for treatment times of 5 min or 30 min, respectively. Thus, the temporal resolution was 0.25 s or 1 s, respectively. Post-processing of the images was done as follows. To obtain the total absorbance, the absorbance signal was averaged over the investigated wavelength range. Depth profiles were created by obtaining the mean value of a 3 mm interval around specific depths. For example, the measurement at a depth of 4.5 mm was averaged from 3 mm to 6 mm. To smooth the noise of the data due to the high temporal resolution, a running mean of 30 was used for all times examined.

2.3. PIV

PIV is a method of tracking particles in a fluid to visualize flow patterns. The laser-driven light source (Energetiq EQ99X-FC) was used. A lens parallelized the light beam and a slit narrowed the light beam to a width of less than 1 mm in diameter. The height of the light beam was 30 mm to cover the entire depth of the liquid. Polyamide particles with a diameter of 55 μm (LaVision) were added to distilled water and were used as scattering particles. To observe the scattered light, a fast-imaging camera (Phantom VEO 410L) was mounted perpendicular to the light beam. The camera was operated with an exposure time of 1900 μs and a sample rate of 500 fps. 1000 images were recorded for every treatment. Post-processing analysis of the images was performed using the open-source Python package OpenPIV [34]. In post-processing, the movement of the particles from one image to the next is tracked and the position of the particles is determined by the cross-correlation method. From the determined vector of particle movement and the time between the two images, the velocity vector of the particles is obtained. More details about PIV can be found in [35]. PIV has been used in several studies to track motion in plasma-treated liquids using dielectric barrier discharge (DBD) plasmas [7, 36], plasma in liquid configurations [37–39], kHz plasma jets [40, 41] and the COST plasma jet [16] with the last being comparable to the plasma jet used in this work.

2.4. OH detection: CL of luminol

The CL of luminol (3-aminophthalhydrazide, $C_8H_7N_3O_2$) [42, 43] was used to detect plasma-generated OH in the liquid. Luminol is mainly excited by the superoxide anion O_2^-, which can be produced in plasma-treated liquids via [42, 44]

$$OH + H_2O_2 \rightarrow O_2^- + H_3O^+. \qquad (1)$$

However, the CL signal was found to correlate with OH-selective terephthalic acid (TA) dosimeter in plasma-treated liquids [45] and with OH measurements in gas phase by laser-induced fluorescence [46]. In a recent publication, we were also able to show the correlation between the TA dosimeter and the CL of luminol in the plasma jet-liquid system studied here [25].

The setup for detecting the CL signal is shown in figure 1(c). A 5 mM luminol solution (Serva Electrophoresis) prepared in distilled water was used. The CL signal was observed *in situ* using an iCCD camera (Andor iStar) with a filter (424 nm, FWHM 10 nm) in front of the camera since the CL spectrum peaks at 425 nm. The exposure time was set to 2 s and accumulated over 5 images, resulting in a total measurement time of 10 s. For each treatment, a reference image was acquired with water only. The CL signal was determined by subtracting the reference image from the CL image as shown in [25].

3. Computational details

3.1. Reactive MD simulations

All MD simulations in this work have been performed with the LAMMPS simulation package (version 23 June 2022 stable release) [47, 48] employing a ReaxFF potential as originally developed by van Duin [23]. ReaxFF is a force field scheme that uses interatomic distances to determine bond orders, which are then used to compute the potential energy function. As such it allows for dynamic bond breaking and formation.

Since the choice of the right interatomic potential or force field is crucial for the quality of the results of MD simulations, several different reactive force fields were tested for their water parameters and the formation energies of the plasma-generated species. The results indicated that the *water2017* [49] and the *protein2013* [50] force fields are closest to experimental values in terms of water density, self-diffusion of water, and water entropy. For the final investigations, the *protein2013* was chosen because the *water2017* force field does not favour H_2O_2 as a stable molecule, since it was specifically trained on water parameters. More details are provided in the supporting information. For the diffusion study, a cubic simulation box ($40 \times 40 \times 40$ Å) was first equilibrated with 2000 water molecules at 300 K with periodic boundary conditions, before adding the reactant molecules (H_2O_2 or OH) to the box. Each simulation ran in an canonical ensemble, in the following referred to as *NVT* ensemble, where *N* is the number of particles, *V* the volume and *T* the absolute temperature. A Langevin thermostat [51, 52] was applied and the simulation ran for a total of 225 ps with a time step of 0.15 fs to correctly model the oscillations of the water's hydrogen. The simulation were repeated three times with different starting conditions, to gain statistical evidence.

For the shooting simulations, 50 000 water molecules were equilibrated in a cubic box with periodic boundary conditions

J. Phys. D: Appl. Phys. **58** (2025) 135208

H-F Poggemann *et al*

(80 × 80 × 180 Å) at 300 K. After equilibration, additional vacuum was added on one side of the box and the last layer of the water structure was fixed. This method was used to prevent the water cluster from moving in the box. The boundary conditions where changed to be non-periodic in *z*-direction and reflective walls were added on the top and on the bottom to prevent loss of atoms. Another equilibration run was performed until a stable water surface had formed. The final shoot simulations were carried out in an *NVT* ensemble again with a Langevin thermostat at 300 K only on the water molecules, so that the reactant molecules, which were shot vertically on the water surface, were not directly influenced by the thermostat. Due to high computational cost each of the shooting simulations was only performed once. The subsequent analysis of the species in the simulation box was performed with the bond order based species analysis algorithm implemented in ReaxFF. Additionally, the results were compared to a species analysis performed with the TRAVIS trajectory analyser [53, 54]. However, it should be noted that the identification of species as a cluster or individual molecules depends on the selected cutoff parameters.

3.2. Kinetic modelling — mass transport with reaction kinetics

Simulating the behaviour of H_2O_2 and OH using MD simulations allows for the investigation of the transport up to the nanosecond time scale. The experimental behaviour is measurable in the time scale of seconds to minutes. Connecting the MD-simulated and experimentally measured results, the kinetic model allows for the system to be simulated over long time scales, bridging the gap between MD-simulations and experiments.

The behaviour of H_2O_2 and OH in the kinetic model is investigated using the spatially one-dimensional (*z*) reaction–diffusion equation

$$\frac{dn_{i,\text{liq}}}{dt} = R_i + D_{i,\text{liq}} \frac{d^2 n_{i,\text{liq}}}{dz^2} \tag{2}$$

where $n_{i,\text{liq}}$ represents the concentration of species *i* in the liquid, R_i the reaction term including producing and consuming reactions of species *i* interacting with the other species, and $D_{i,\text{liq}}$ the diffusion coefficient of species *i* in the liquid. In this work, different values are used for this coefficient for H_2O_2 based on those inferred from MD simulations and experiment, as discussed later. Briefly, the diffusion coefficients from the MD simulations can be interpreted as the molecular diffusion coefficient, representing purely diffusive transport. Those measured in the experiment are likely to include other transport processes, as discussed later. Therefore, these values are more representative of an effective diffusion coefficient. In this work, such an effective diffusion coefficient for H_2O_2 could be measured in the experiment at the lowest gas flow rate used, but not for high gas flow rates, as discussed in more detail later. Therefore, only the low gas flow rate case is studied using the kinetic model. As an effective diffusion coefficient for OH could not be measured experimentally, the molecular diffusion coefficient from the MD simulations is always used for

Table 1. Chemical reactions included in the model [55].

No.	Reaction	Rate coefficient $m^3 s^{-1}$
1	$OH + OH \rightarrow H_2O_2$	1.7×10^{-17}
2	$OH + H_2O_2 \rightarrow HO_2 + H_2O$	1.0×10^{-19}

OH. The reaction–diffusion equation is solved on a spatial-temporal (*z*-*t*) mesh for a simplified reaction network including two species considering two reactions (table 1). In general, the overall reaction network related to OH and H_2O_2 is expected to be much larger, as shown in [55, 56], for example. However, these two reactions are known to be particularly important, and are sufficient for this study which is mainly focused on transport effects.

The initial condition of each species is a concentration of 1.661×10^{-17} M (1×10^{10} m^{-3}), to approximate a case where the densities of OH and H_2O_2 are effectively zero at the start of the simulations when the plasma is turned on. The first boundary condition at $z = 0$ mm requires flux conservation at the liquid surface and is implemented based on transport across a diffusion boundary layer above the liquid surface. The expressions used are detailed below and are taken from the work of Semenov *et al* [59], who used them to interpret the results of 2D fluid simulations of reactive species transport at gas–liquid interfaces. Importantly, these expressions allow for the relative importance of convection and diffusion driven transport across the interface to be included, which is important for our cases where an active gas flow is applied by the jet to the liquid interface. The diffusion flux at the liquid side of the interface is equal to the flux entering the liquid from the gas phase:

$$D_{i,\text{liq}} \frac{dn_{i,\text{liq}}}{dz} = \gamma n_{i,*} v_{i,*}. \tag{3}$$

Here, the flux at the gas phase side of the interface in the *z*-direction is defined as a coefficient γ times the characteristic species density delivered from the jet at the edge of the boundary layer $n_{i,*}$ and the characteristic gas velocity normal to the liquid surface at the edge of the boundary layer $v_{i,*}$. The gas velocity is assumed to decrease linearly from the plug-flow value at the exit of the glass capillary (see description of experimental setup), to a value of zero at the gas–liquid interface. The value of $v_{i,*}$ is taken to be the value of this linear function at the edge of the diffusion boundary layer, whose width is defined by $\delta_{i,*}$ below. The coefficient γ is defined as

$$\gamma = \frac{1 - \frac{n_{i,\text{liq}}}{H_{i,S}^{CC} n_{i,*}}}{1 - \exp(-Pe) + \frac{Pe}{\alpha}} \tag{4}$$

where $H_{i,S}^{CC}$ is the Henry's law solubility constant of species *i*, *Pe* is the Peclet number in the diffusion boundary layer of the gas phase, given as

$$Pe = \frac{n_{i,*} \delta_{i,*}}{D_{i,\text{gas}}}, \tag{5}$$

Table 2. Neutral species densities in the gas phase $n_{i,\text{gas}}$ simulated using a pseudo-1D plug-flow model in GlobalKin [55], diffusion coefficient in the liquid $D_{i,\text{liq}}$ (MD-simulated and for H_2O_2 experimentally obtained) and in the gas phase $D_{i,\text{gas}}$ [58], and Henry's law solubility constant $H_{i,S}^{\text{CC}}$ of the species (i) [55]. The diffusion coefficient of H_2O_2 is changed between the [e] experimentally measured effective diffusion coefficient and [MD] MD-simulated molecular diffusion coefficient. The coefficient α is calculated using the diffusion coefficient from the MD simulation.

Species i	$n_{i,\text{gas}}$ m^{-3}	$D_{i,\text{liq}}$ m^2 s^{-1}	$D_{i,\text{gas}}$ m^2 s^{-1}	$H_{i,S}^{\text{CC}}$ dimensionless
OH	9.651×10^{15}	1.02×10^{-9}	4.0×10^{-5}	6.2×10^2
H_2O_2	9.363×10^{20}	[e] 2.6×10^{-8} | [MD] 6.0×10^{-10}	2.0×10^{-5}	1.92×10^6

and the coefficient α given as

$$\alpha = \frac{D_{i,\text{liq}}^{(\text{MD})}}{D_{i,\text{gas}}} \frac{\delta_{i,*}}{\Delta} H_{i,S}^{\text{CC}}. \qquad (6)$$

Note that the liquid diffusion coefficient used in this expression is always the molecular diffusion coefficient from the MD simulations, as the coefficient α deals with transport in the liquid boundary layer where enhanced transport due to convection is not expected, as discussed in Semenov *et al* [59]. The Peclet number and the coefficient α both depend on the width of the diffusion layer δ_* which is, in this study, set to 1 mm while the thickness of the viscous sublayer in the liquid phase Δ is set to 10 μm. Both values are estimates, and are assumed here to be in the same range as those used by Semenov *et al* [59]. This is motivated by the similar gas flow conditions in this work compared to that of Semenov *et al* [59]. The gas phase densities (table 2) used as the characteristic species density delivered from the jet $n_{i,\text{gas}}$ are obtained from plasma-chemical kinetics plug-flow simulations using GlobalKin [55] for the capillary plasma jet operated with helium [14, 57] and a 6400 ppm water admixture. The simulations are performed for a gas flow velocity of 0.25 slm. The length of the effluent outside the capillary is defined considering the decrease of the flow velocity with distance from the exit of the capillary. This results in a longer time to pass the free effluent region of 13 mm until the beginning of the diffusion boundary layer and therefore a longer plug flow simulation distance compared to the case where the velocity decrease in the effluent is not considered. Simulations are carried out for time periods when the plasma is switched on, and off to replicate the conditions studied in the experiment. When the plasma is switched on the input power to the simulations is set to 6 W to calculate the gas phase densities of plasma produced species. For times when the plasma is turned off in the experiment, the diffusion flux at the gas–liquid interface is set to 0. The second boundary condition at the bottom of the cuvette ($z = 30$ mm) is defined by a constant flux.

The diffusion equation is solved in MATLAB using *pdepe* [60]. In order to achieve a stable solution of the PDE system even at extremely low species densities, which occur for OH at large depths within the liquid, a very small artificial constant generation rate of OH of 1 m^{-3}s^{-1}, which is negligible as soon as larger steady-state densities are reached, was added. In the following, the model considering mass transport and reaction

kinetics is denoted as kinetic model, to distinguish it from the MD simulations.

4. Results and discussion

4.1. Experimental investigation of OH and H_2O_2 distribution in plasma-treated water

In a liquid treated by an atmospheric pressure plasma jet, transport occurs due to the slower diffusion of reactive species and the faster convection due to the mixing of the liquid. Chemical luminescence is a possible diagnostic method for visualizing reactive species and their distribution in the liquid. In this work, luminol was used to observe the CL of the OH radical.

The CL signal of luminol during plasma treatment is shown in figure 2(a) for three different gas flow rates. In all cases, a distinct CL signal can be observed at the liquid surface. At a gas flow rate of 2 slm, the intensity of the CL signal is uniformly distributed over the surface, but a pronounced dip of up to 5 mm can be seen in the centre of the liquid surface, where the capillary, and thus the gas flow, faces the liquid. The dip is created by the interaction of the gas with the liquid surface since momentum transfer is greater at higher gas flow rates. At lower gas flow rates, the dip vanishes and the intensity is no longer evenly distributed, but is strongest in the centre and decreases toward the sides. However, in all cases, the CL signal is only visible up to 2 mm beneath the liquid surface. This depth can be used to discuss transport phenomena of OH in the plasma-treated liquid.

However, in discussing possible diffusion processes of OH, the origin of the CL signal must first be discussed. Luminol is excited by the superoxide anion O_2^-. In plasma-treated liquids, the anion is produced via the reaction between OH and H_2O_2 (see equation (1)) with typical timescales of a few microseconds. In the next step, the CL occurs from the de-excitation of the excited luminol. The temporal behaviour of the excitation and de-excitation can be determined from an ordinary differential equation given in [44]. The calculation and the results are shown in the SI. Excitation of luminol takes only a few microseconds, while de-excitation takes up to a few milliseconds. The CL observed in the experiments is made up of three processes: the production of O_2^-, the excitation of luminol, and its de-excitation. Since de-excitation is the slowest process, CL represents diffusion of the excited luminol rather than diffusion of the OH radical. Nevertheless, OH must
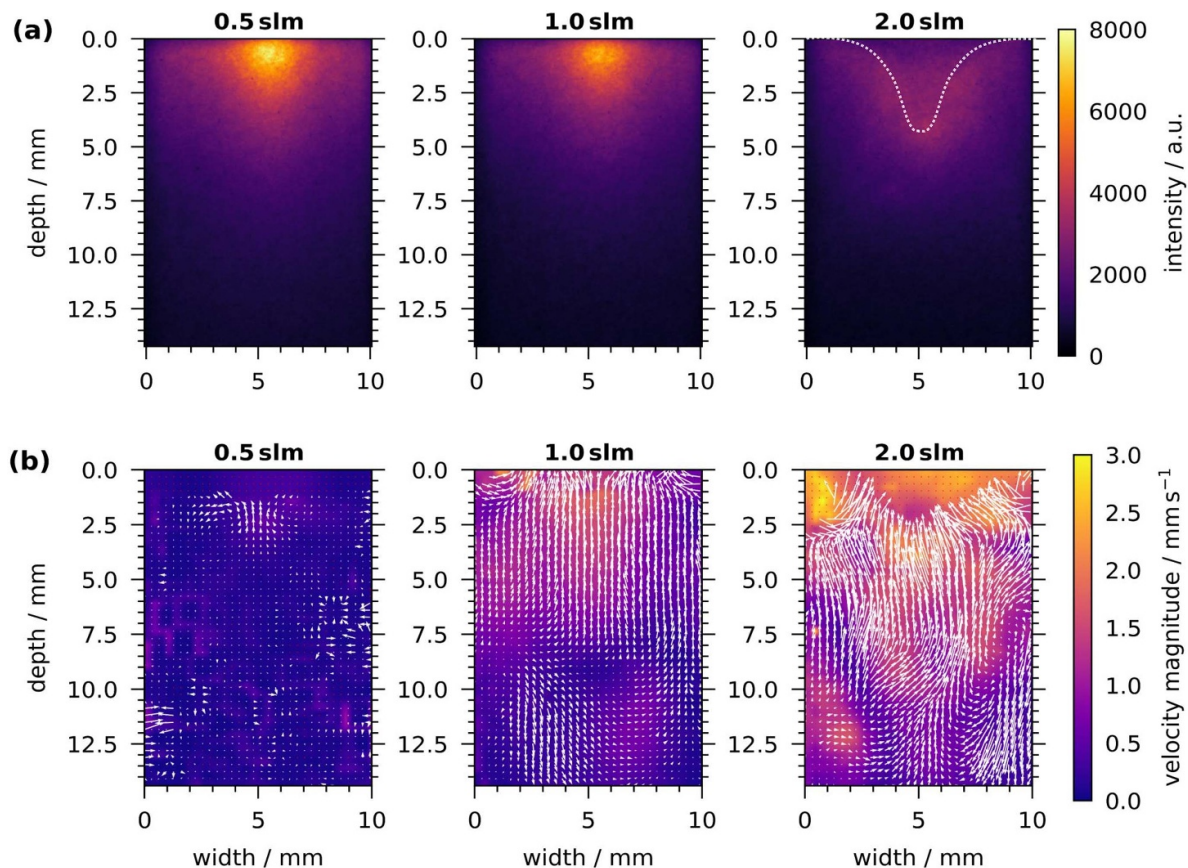
Figure 2. (a) Chemiluminescence of luminol to visualize the distribution of OH in plasma-treated water for gas flow rates of 0.5 slm, 1 slm and 2 slm. Plasma was operated at 6 W and a humidity of 640 ppm. Dashed line at 2 slm illustrates the shape of the liquid surface. (b) PIV images under plasma treatment for the three gas flow rates. The liquid surface before plasma treatment is present in all images at 0 mm. Liquid surface is located at 0 mm in both methods.

be present to excite the luminol. Since no CL is visible below 2 mm, no OH is likely present below 2 mm, and the depth of the CL signal can be used as an upper limit for the diffusion of the OH radical. With a depth of 2 mm and an integration time of 10 s of the measurements, the diffusion coefficient of OH can be estimated to be less than 2×10^{-7} m^{2}s^{-1} from the average distance travelled per time.

Convection in a plasma-treated liquid by a plasma jet is mainly driven by friction. The gas flow hits the liquid surface and travels along the surface. Due to friction, the liquid is accelerated towards the sides and an induced liquid motion is created. In this way, reversed vortices are created at the side of the vessel with an upstream phase in the centre. This has been investigated in experiments [15–17] and modelling [18–21].

In the plasma–liquid system investigated in this work, this reversed vortex pattern is also visible, as shown in figure 2(b). At a gas flow rate of 2 slm the velocity in the liquid reaches values up to 3 mm s^{-1}, while at 1 slm it drops to 1 mm s^{-1}, and at 0.5 slm practically no vortex pattern or liquid motion is visible. Convection is thus strongest at high gas flow rates and is impeded at low gas flow rates of 0.5 slm and less.

This flow pattern might also explain the lower intensity of the CL signal at high gas flow rates. The CL measurement is accumulated for 10 s and with a higher gas flow rate, and thus

a stronger convective transport, the excited luminol is distributed more towards the liquid surface, leading to a lower intensity. However, since the CL signal is only located at the liquid surface at the three different gas flow rates, the transport of OH can be attributed to the diffusion of OH into the liquid rather than convection. If it were driven by convection, the CL signal would be more deeply distributed at higher gas flow rates, but this is not the case.

The transport of H$_2$O$_2$ was investigated by 2D UV absorption spectroscopy in the liquid. Example images of the absorbance are shown in the SI, while depth profiles of the total absorbance from 237 nm to 271 nm are shown in figure 3, for a treatment time of 5 min at three different gas flow rates.

At a gas flow rate of 1 slm (middle part of the figure), the absorbance increases immediately after the start of plasma treatment and increases at all depths. Some fluctuations are visible, but these can be attributed to dust particles and impurities in the cuvette, as they are already visible with a pure gas flow and no plasma (details in SI).

At the highest gas flow rate of 2 slm, the same trend is evident, and absorption increases at the same rate at all depths investigated. After about 140 s, the increase in absorption at a depth of 4.5 mm is enhanced compared to the other depths. This is due to evaporation, as the evaporation increases with
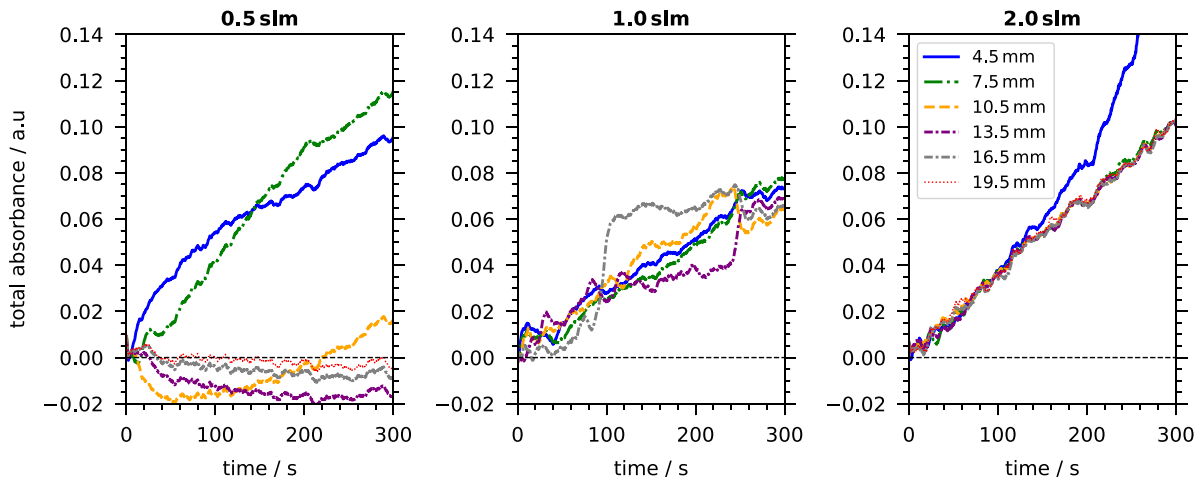
Figure 3. Total absorbance from 237 nm to 271 nm of plasma-generated H_2O_2 over treatment time for gas flow rates of 0.5 slm, 1 slm and 2 slm at various depths within the liquid. Plasma was operated at 6 W and a humidity of 6400 ppm. Legend is true for all. Please note that the depth of 19.5 mm could not be evaluated for the case of 1 slm due to disturbances.
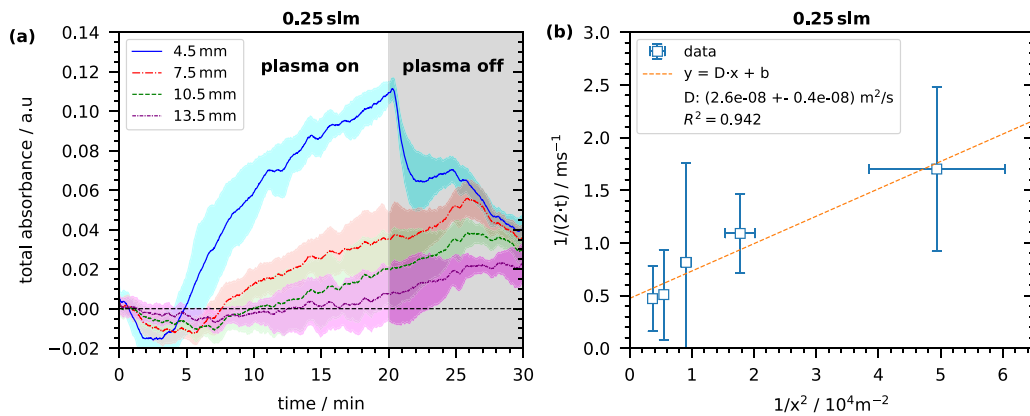

Figure 4. (a) Total absorbance from 237 nm to 271 nm of plasma-generated H_2O_2 over treatment time for a gas flow rate of 0.25 slm at various depths within the liquid. Mean (lines) and standard deviation (shaded area) of three measurements are shown. Individual measurements are shown in SI. Plasma was operated at 6 W and a humidity of 6400 ppm. (b) Plot of $1/(2t)$ as a function of $1/x^2$ to determine the effective diffusion coefficient, which is given by the slope of the linear fit.

increasing gas flow rate and thus the measurement is no longer in the liquid but in the gas phase. This could be observed after the treatments, as the liquid surface was below the upper edge of the light beam. Thus, the reference is no longer accurate and the measurement is no longer trustworthy.

As shown above, strong convective transport is present at high gas flow rates with velocities in the liquid in the order of millimetres per second. Thus, it is clear that the absorption of H_2O_2 in the liquid increases at all depths at high gas flow, since the convectional transport is fast and dominates under these conditions.

Remarkable differences in absorption at different depths can be observed at a gas flow rate of 0.5 slm. Near the liquid surface (4.5 mm below the liquid surface) the absorption increases immediately. It takes about 50 s for the absorption to also increase at the next depth of 7.5 mm. At even greater depths, the signal is initially negative, due to misalignment of the setup caused by lowering of the plasma jet, but it takes even longer to exhibit an increase in absorbance. Since it takes 5 min

to measure absorption at a depth of 10.5 mm, a longer measurement was made and the gas flow rate was reduced even to 0.25 slm. The results are shown in figure 4(a) as mean and standard deviation of three measurements. There, the same trends can be seen. The absorption first increases at a depth of 4.5 mm after 5 min, then at 7.5 mm after 7 min and even later with increasing depth. Turning off the plasma after 20 min leads to a decrease in absorption at 4.5 mm depths, while at the other depths, the absorption still increases.

As a result of the slower transport at 0.25 slm, due to the decreased effect of convection, it is possible to carry out a more quantitative analysis of the transport rate. To investigate the behaviour quantitatively, the starting point of absorption, defined as the time at which absorption is greater than zero, was analysed. From this analysis, a diffusion coefficient of H_2O_2 in the liquid can be determined. However, since convection still occurs weakly even at low gas flow rates, the value obtained represents an effective diffusion coefficient, valid only for the specific conditions under which it

is measured. This effective diffusion coefficient is a convolution of contributions from molecular diffusion, convective transport and other mechanisms such as gravity. It is used later to quantify the rate of transport of H_2O_2 in the liquid in the experimental system under these specific conditions, and link the kinetic model with the experimental measurements. In figure 4(b), $1/(2t)$ is plotted as a function of $1/z^2$ in accordance to the determination of an effective diffusion coefficient from Einstein–Smoluchowski-equation:

$$D_{liq}^{e} = \frac{z^2}{2t}, \tag{7}$$

with the effective diffusion coefficient D_{liq}^{e}, time t and distance (here depth) z. A linear increase with a slope of $(2.6 \pm 0.4)\,10^{-8}\,\mathrm{m^2 s^{-1}}$ is evident. This slope is equivalent to an effective diffusion coefficient for H_2O_2 in the plasma-treated liquid at 0.25 slm gas flow rate. Since the gas flow is still present, the convective transport is not completely avoided but minimized. The obtained diffusion coefficient by UV absorption is still a combination of both, pure diffusion and convection. This also explains why the experimentally obtained effective diffusion coefficient of H_2O_2 is larger than the molecular diffusion coefficients obtained by MD simulations (presented in the next section) and the literature.

Furthermore, the observed trends fit well with previously published works [33, 61]. Liu *et al* studied the distribution of reactive oxygen and nitrogen species by UV absorption spectroscopy in a liquid treated with a DBD plasma [33]. The DBD was operated in the atmosphere, so no gas flow and thus limited convective transport was present. They found similar timescales of 100 s for a transport path of 5 mm.

To conclude the experimental analysis, OH is predominantly present at the liquid surface and is less transported through the liquid as it reacts at the liquid surface. Convective transport is present at gas flow rates of 1 slm and higher. In the case of H_2O_2, convective transport leads to a homogeneous distribution of H_2O_2 through the liquid to a depth of 20 mm. However, transport of H_2O_2 towards increasing depths in the liquid could only be effectively visualised at low gas flow rates (0.5 slm and less). An effective diffusion coefficient of $(2.6 \pm 0.4)\,10^{-8}\,\mathrm{m^2 s^{-1}}$ for H_2O_2 was determined at a gas flow rate of 0.25 slm.

4.2. Molecular dynamic simulation

4.2.1. Diffusion of OH and H_2O_2 in aqueous environment.
The diffusion behaviour of two plasma species, namely OH and H_2O_2, in water has been studied in detail.

To determine the diffusion coefficient of each species in water, the mean squared displacement was calculated from the MD simulation trajectory and fitted linearly. For pure water, a diffusion coefficient of $(1.2 \pm 0.026)\,10^{-9}\,\mathrm{m^2 s^{-1}}$ was obtained. This value is close to the experimental value of $2.31 \times 10^{-9}\,\mathrm{m^2 s^{-1}}$ from Krynicki *et al* [62] (for comparison the literature values are also shown in figure 5) and nearly identical to a similar study from Yusupov *et al* [22].

The diffusion coefficient of H_2O_2 in water was found to be $(6.0 \pm 0.90)\,10^{-10}\,\mathrm{m^2 s^{-1}}$, which means that H_2O_2 diffuses more slowly than the self-diffusion of water. This result is also in accordance with the calculated value from M Yusupov *et al* [22]. The Arrhenius plot in figure 5 shows the temperature-dependent diffusion behaviour of H_2O_2 in blue. As expected, with increasing temperature the H_2O_2 molecules in solution move faster and have, therefore, a higher diffusion coefficient. As shown in figure 5(b) H_2O_2 has a limited diffusion radius in water and moves relatively little in comparison to OH, which is highly mobile in the liquid, as illustrated in figure 5(c). The diffusion coefficient of OH is almost identical to the self-diffusion of water (see red data points in figure 5), which was to be expected, since OH is strongly involved in the proton-hopping processes of the water structure, also known as Grotthuss mechanism [63].

Both species have an activation energy for the self-diffusion that is close to the activation energy of water self-diffusion [62]. In addition to the different temperatures, the influence of species concentration on the diffusion was tested. Up to a concentration of 1/20 species ratio this does not affect the diffusion coefficient.

In summary, the MD simulations of the bulk liquid underlined the expectation that the diffusion of H_2O_2 and OH is dominated by the self-diffusion of water, since both species have a similar size to the solvent.

4.2.2. Lifetime in water.
The lifetime of the plasma-generated species in water was studied as a function of temperature, as well as initial concentration. As shown in figure 6(a) for H_2O_2 at 278 K the initial concentration of 100 molecules decays to about 80 molecules in 225 ps, and at 363 K the concentration drops to 60 molecules. The lower temperature shows a slower decay compared to 363 K, but a clear temperature dependence could not be extracted from the tested temperatures in between.

It is known from the literature that H_2O_2 is not stable in water for long times, especially at room temperature or higher temperatures [64]. However, the concentration loss in the simulations appeared to be higher than expected with nearly 50% in less than half a nanosecond. For this reason, an additional concentration-dependent study was conducted.

The lifetime of H_2O_2 in water seems to be influenced strongly by the initial concentration of the species. As shown in panel (b) of figure 6 at an initial amount of 100 H_2O_2 molecules in solution the number of molecules decreases to about 70. With 50 molecules initially, the amount is almost stable throughout the total simulation time. This concentration study shows, the rapid decay of H_2O_2 molecules is an effect of the high concentration. H_2O_2 seeks an equilibrium concentration in aqueous environments where the amount of molecules is constant over time. Because of that the lower initial concentration of 50 molecules shows no fluctuations, it seems to be below the equilibrium concentration and therefore all H_2O_2 molecules remain intact. Of course, these absolute numbers
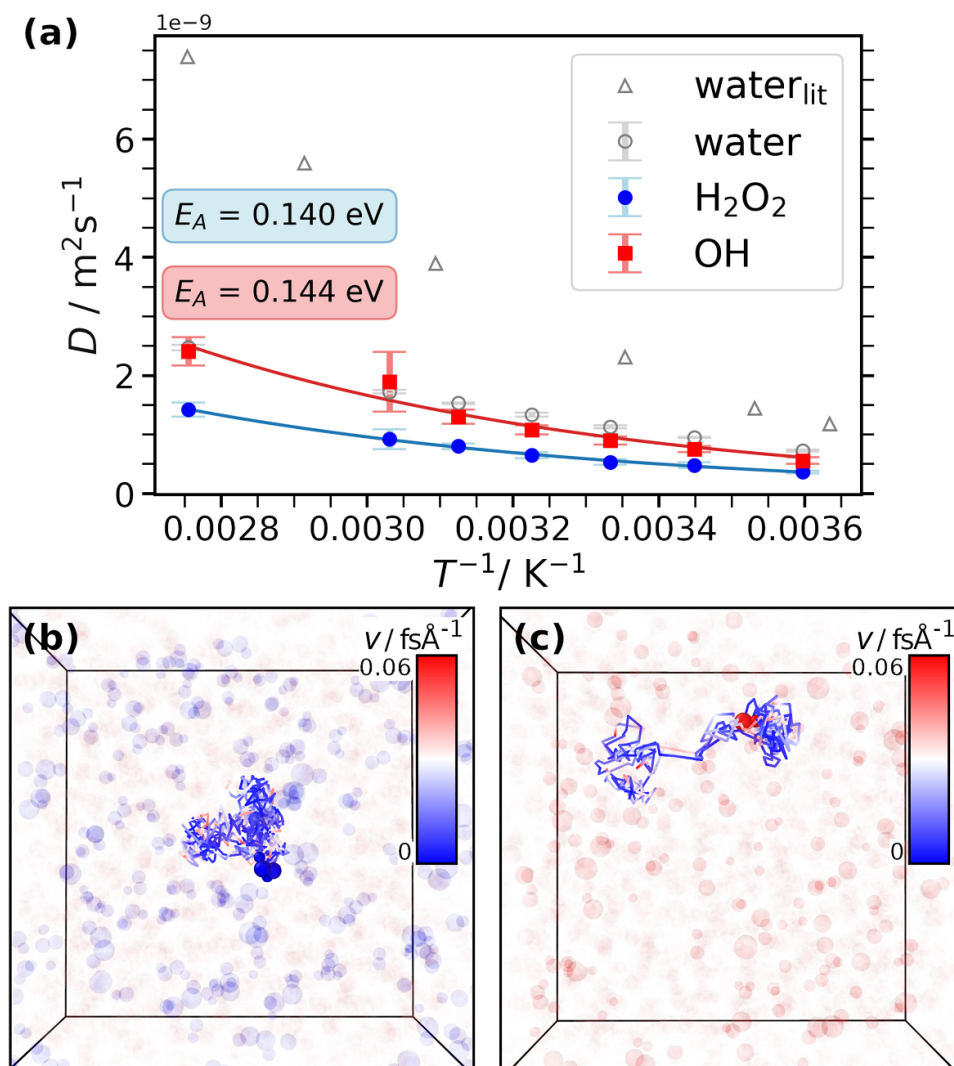
Figure 5. (a) Temperature-dependent diffusion coefficient of water (grey triangles: experimental values from Krynicki *et al* [62], grey circles: simulation values), solvated H_2O_2 (blue) and OH (red) plotted in an Arrhenius plot. The panels (b) and (c) show schematically the diffusion path of a single H_2O_2 molecule or OH molecule in solution, respectively.
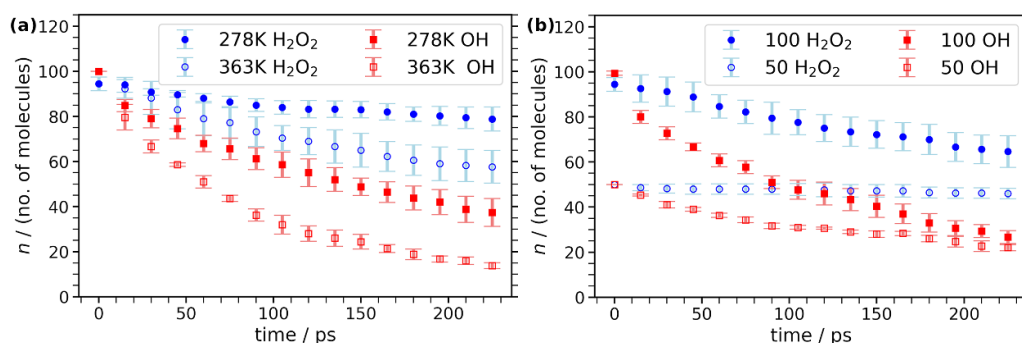

Figure 6. Lifetime of solvated species under different conditions. H_2O_2 is shown in blue circles and OH in red squares. (a) Number of species molecules versus time at 278 K and 363 K, respectively. (b) Number of species molecules versus time with different initial concentrations at a temperature of 300 K.
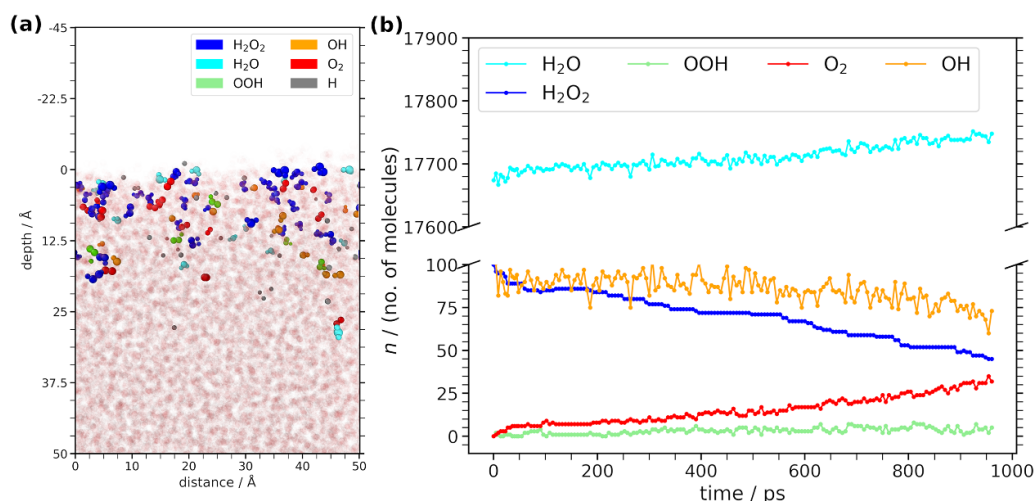
Figure 7. (a) Simulation snapshot at 1 ns simulation time, showing the dissociation products of H_2O_2 mostly on the water surface. The different colours indicate the species. (b) Species analysis of solvent and 100 H_2O_2 molecules over time.

should be treated with care, since the MD simulations were performed at a high concentration in a system of very limited size. Even through repetition with different starting conditions, over the short simulation time only a conditional measure of statistics is possible. However, the trend of the study is valid. High concentrations lead to a shorter lifetime and more dissociation into other species. In the context of the experimental studies, the low concentration results are of greater importance. Few dissociation reactions will occur in the studied system, and the H_2O_2 concentration can be considered stable.

A species analysis at the end of all simulations shows that H_2O_2 if H_2O_2 dissociates, it mainly dissociates to H and OOH. Most of the H atoms interact with the surrounding liquid to form water (figure 11(a) in the SI). Dong *et al* [64] found similar results and declared the H–OOH channel as the favourable decomposition pathway for H_2O_2 in water.

In comparison to H_2O_2, the amount of OH decreases faster and after 225 ps there are only about 20 of 100 initial molecules left in the simulation box (figure 6(b)). But again with an initial amount of 50 molecules the species is more stable. Thus, the extreme decay is probably an effect of the high concentration. However, solvated OH interacts strongly with water, forms clusters and participates in proton hopping processes following the Grotthuss mechanism [63]. This behaviour is reproduced in the MD simulations, but OH–H_2O clusters or transition states are not considered in the species analysis. Therefore, the species analysis gives the impression that less OH is present in the system than is actually the case. Additionally, the simulation results of OH, as seen in figure 6(a), indicate a correlation between the temperature and the rate of decay.

4.2.3. Shooting simulations. Similar to the experimental setup, large scale MD simulations were performed, in which single plasma species molecules were shot onto an equilibrated water surface to observe diffusion into the bulk

water. The plasma species had an initial velocity of 0.01 Å fs^{-1} ($100\,000\ ms^{-1}$) in *z*-direction. This value is significantly higher than experimental thermal velocities of a few 100 ms^{-1} but slower velocities were not reasonable on MD time scales. The simulations showed that a single H_2O_2 molecule barely diffuses into the bulk water, only about 10 Å over a time period of 1 ns. The molecule loses all of its kinetic energy the moment it hits the water surface. The relation between the impact velocity and the self diffusion of water plays a crucial role here. The faster the molecule is accelerated towards the surface the less time the water molecules have to move. Consequently, the surface behaves like a solid body and the H_2O_2 molecule then 'floats' on the surface for an extended period of time before slowly diffusing into the bulk. When more molecules are shot onto the water surface at once, for which several simulations were performed in increments of 10 to 100 molecules, the total diffusion of H_2O_2 into the bulk is deeper (figure 7(a)). A detailed list of the acquired values can be found in table 5 in the supporting information. The increased diffusion into the bulk can be explained by the stronger turbulence of the water surface when several molecules hit the surface. The network structure of the water molecules is broken more frequently, making it easier for the H_2O_2 molecules to diffuse deeper into the bulk. Nevertheless, over a period of 1 ns, most H_2O_2 molecules remain on the surface. Therefore also the diffusion coefficient of H_2O_2 on the surface ($2.043 \times 10^{-10}\ m^2 s^{-1}$ for 100 molecules) is higher than in the bulk. In terms of implications for the experimental measurements 4.1, we can conclude that, under experimental conditions where velocities are much lower, most plasma species will lose their initial velocity upon impacting the water surface. Consequently, their movement into the bulk water is not driven by ballistic motion but rather by other transport mechanisms, such as diffusion and convection.

Interestingly, the stability of the species is not affected significantly by the collision with the water surface, despite the high acceleration to the surface. However, the simulations showed that nearly half of the H_2O_2 molecules dissociate over

time. They mostly reform to H_2O and O_2. The species analysis (figure 7(b)) also shows a high concentration of OH in the simulation box. Partially they might come from H_2O_2 dissociation, but most of them are due to the liquid environment. Again, these results should be treated with care, as the concentrations used in the MD simulations are larger than the experimental values.

The results for OH are very similar to H_2O_2. Both species show comparable maximum diffusion depths after 1 ns of total simulation time and, again, most molecules remained on the water surface. The maximum diffusion depth also increases with the number of molecules shot onto the water surface. As for H_2O_2 the dissociation products are the same as in the bulk water simulations and the diffusion coefficients of the species are slightly increased compared to the bulk diffusion.

4.3. Kinetic simulation of the OH and H_2O_2 behaviour in water for different diffusion coefficients of H_2O_2

The behaviour of H_2O_2 at a gas flow rate of 0.25 slm is investigated by one-dimensional liquid simulations using the MD-obtained molecular diffusion coefficient and the experimentally determined effective diffusion coefficient as input, to compare the observed behaviour and bridge the gap between the time scales of the two methods. The kinetic simulation solves the reaction–diffusion equation as mentioned in section 3.2 starting in the range of the MD-simulations (0.1 ns) up to the experimental time scale (1200 s). Only the low gas flow rate of 0.25 slm is considered here as this is the only case for which an effective diffusion coefficient could be determined experimentally.

4.3.1. Species behaviour and influence of the diffusion coefficient of H_2O_2.
Solving the reaction–diffusion equation considering a simplified chemical reaction system of two species and two reactions results in the species concentration profile over space and time, as shown for H_2O_2 in figure 8.

The H_2O_2 concentration and the penetration depth increase with treatment time for both diffusion coefficients. The gradual expansion of H_2O_2 in space and time is caused by transport behaviour, whose rate is determined by the value of the diffusion coefficient used. The maximum penetration depth of H_2O_2 for the simulated time frame is in the range of a few millimetres for the MD-simulated diffusion coefficient, while it is an order of magnitude higher for the experimentally obtained value. The difference between these two is that the effective diffusion coefficient from the experiment is 43 times higher than the MD-simulated molecular diffusion value, which determines faster penetration but also impacts the distribution of H_2O_2 in the liquid. The vertical lines indicate the in figure 9 visualised points in time at (dotted) $1\,\mu s$ and (dashed) 200 s.

At $1\,\mu s$ (figure 9 - solid black and dashed red lines), the overall behaviour of the species is defined by the flux of the species entering from the gas phase and the diffusion coefficient. Since both species have a different diffusion coefficient, the maximal penetration depth varies between each species. Also, the flux of each species influences the penetration depth. This depends on the species density in the gas phase and on the solubility. OH and H_2O_2 first show a nearly constant behaviour, and later on a fast decrease. The effects of a faster penetration and the impact on the distribution of H_2O_2 in the liquid, as mentioned above for figure 8, for the experimentally obtained effective diffusion coefficient are recognisable by evaluating the H_2O_2 behaviour (a) at $1\,\mu s$, for the experimentally obtained effective value (solid black line) and the MD-simulated molecular diffusion coefficient (dashed red line). The penetration depth of H_2O_2 into the liquid is higher for the experimentally obtained diffusion coefficient (solid black line), while the maximal amount of H_2O_2 is lower compared to the results using the MD-simulated value (dashed red line). The behaviour of OH (b) is thereby not recognisably influenced, which supports the thesis of mainly transport-driven behaviour at these short times i.e. the reaction of OH + H_2O_2 is not playing a major role in the consumption of OH.

(a) $D^e_{H_2O_2} = 2.6 \cdot 10^{-8}\,\mathrm{m^2\,s^{-1}}$ **(b)** $D^{MD}_{H_2O_2} = 6.0 \cdot 10^{-10}\,\mathrm{m^2\,s^{-1}}$
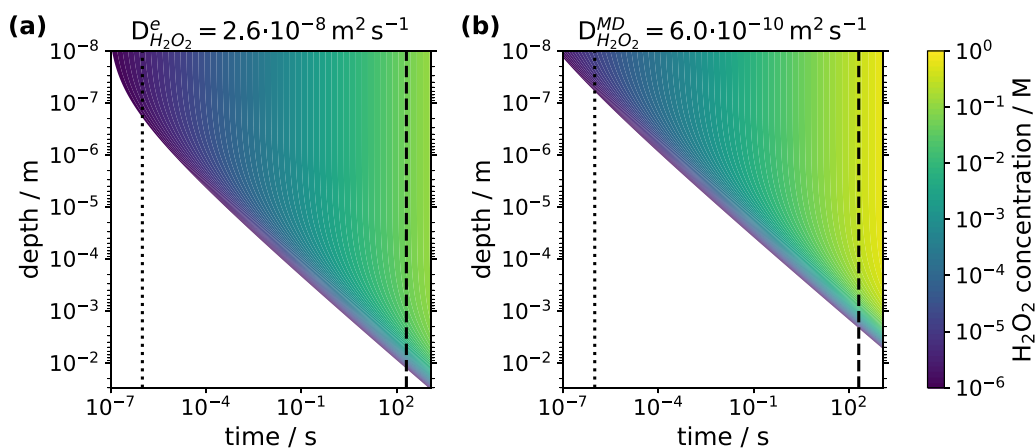
Figure 8. H_2O_2 concentration over (*x*) simulation time (*y*) penetration depth into the liquid for (a) the experimentally obtained effective diffusion coefficient of H_2O_2 and (b) the MD-simulated molecular diffusion coefficient of H_2O_2. The dotted ($1\,\mu s$) and dashed (200 s) vertical lines indicate the in figure 9 visualised points in time.
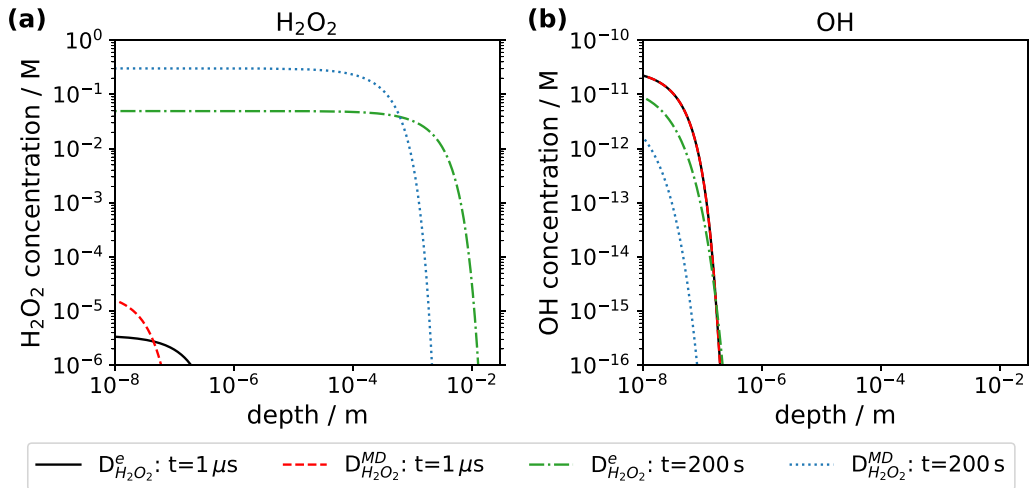
Figure 9. Species concentration of (a) H_2O_2 and (b) OH over penetration depth into the liquid at $1\,\mu$s and $200\,$s simulation time for the experimentally obtained effective diffusion coefficient of H_2O_2 $D^e_{H_2O_2}$ and the MD-simulated molecular diffusion coefficient of H_2O_2 $D^{MD}_{H_2O_2}$. The diffusion coefficient of OH is the MD-simulated molecular diffusion coefficient. Legend applies to both figures.

At $200\,$s (figure 9 - dash-dotted green and dotted blue lines) there is a clear difference between the long-living species H_2O_2 (a) and the short-living species OH (b). The long-living H_2O_2 is mainly driven by the diffusive behaviour, as already mentioned for H_2O_2 in figure 8. The short-living OH is mainly determined by the chemistry and reacts by less than a μm penetration depth into the liquid. Compared to the long-living H_2O_2, the penetration depth into the liquid is around four orders of magnitude lower. Comparing the results using the MD-simulated diffusion coefficient (dashed red and dotted blue lines) to the experimentally obtained value (solid black and dash-dotted green lines), the tendency of higher penetration of H_2O_2 (a) into the liquid is visible for the experimentally obtained diffusion coefficient. The difference in the simulated results between the MD-simulated and the experimentally obtained diffusion coefficient of H_2O_2 is around one order of magnitude.

Overall, the results of the experimentally obtained diffusion coefficient of H_2O_2 show a higher penetration depth of H_2O_2 than the MD-simulated bulk diffusion coefficient. This allows for the assumption that not only diffusion but also other transport mechanisms, such as convection (forced or free convection) or gravity, are measured in the experiment and allow for the estimation of an effective diffusion coefficient including these phenomena.

4.3.2. Comparison to experimental results. The kinetic simulation results of the H_2O_2 behaviour over time at different points in depth compared to the experimental measurements (figure 4) are shown in figure 10. Therefore, 20 min with plasma-delivered species from the gas phase followed by 10 min without plasma impact are assumed.

Here, a good agreement of the overall behaviour in the first 20 minutes (plasma on) at the different depths is visible. The H_2O_2 behaviour at later times after the plasma is switched off shows a comparably higher deviation, particularly for the lower penetration depths of 4.5 mm and 7.5 mm, where the
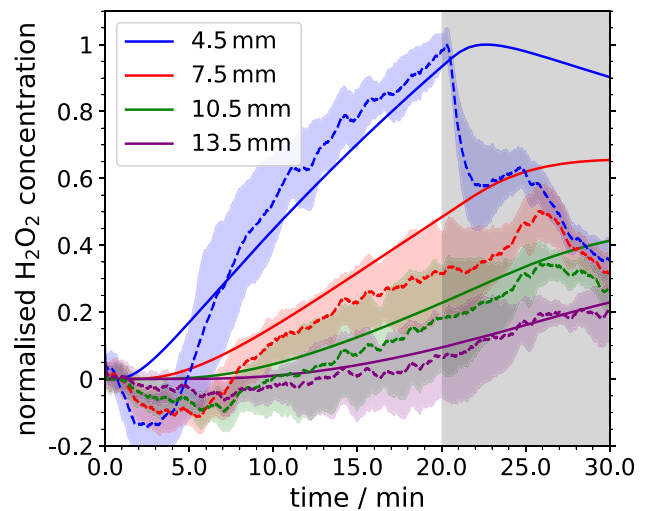

Figure 10. Comparison of the experimentally measured (dashed lines) and simulated (solid lines) normalised H_2O_2 concentration over time at various depths within the liquid. The shaded profiles correspond to the standard deviation of three measurements. The simulations are performed using the experimentally obtained diffusion coefficient of H_2O_2. The first 20 min are with and the last 10 min without plasma impact (grey area).

experimental results show a steeper decrease than the simulated kinetic model results. The difference in the simulated results is likely caused by the simplifications of the kinetic model by including the limited number of species and also neglecting transport in the radial direction in the liquid by diffusion or convection. The influence of the additional effects in the experimental measurements, such as from turning off the plasma and the gas flow, where not all interactions with the surface and the delivery of plasma provided species stop immediately may also play a role. However, as the trends during the plasma on time and deeper in the liquid agree well, the model appears

to provide a reasonable approximation of the transport behaviour of H_2O_2 within the liquid. Further developments of the model to account for radial transport and gas–liquid interactions could further improve the agreement.

The simulated and experimentally measured concentration of H_2O_2 is lower for higher depth since the transport from the liquid surface into the liquid is limited and needs to develop with time. This is also recognisable in the increase of H_2O_2 with treatment time. In the time after the plasma is switched off, the increase of H_2O_2 is still present at first, but changes to a decreasing behaviour as less of the species is delivered from the gas phase into the liquid. Therefore, the decrease starts delayed for higher depths, caused by the same transport behaviour as the delayed increase of the H_2O_2 concentration with depth for earlier times when the plasma is switched on.

Overall, the comparison of the kinetic modelling results with the experimental results indicates the opportunity to predict the species behaviour of H_2O_2 in the real system for a wide range of treatment time and penetration depth. The combination of the purely diffusive behaviour simulated using MD-simulations, with the effective diffusion coefficient measured in the experiment considering other transport mechanisms, as shown in section 4.3.1, such as convection or gravity, allows for a connection between the ideal and the real system. A direct comparison between the experimental measurements of OH penetration and those simulated by the kinetic model has not been carried out as this would require the CL process, used in the experimental measurements, to be included in the model. This is a point to be considered for future work.

5. Conclusion

In summary, the diffusion of OH and H_2O_2 in water under plasma treatment with an atmospheric pressure plasma jet has been investigated by a combination of experimental measurements, kinetic modelling and MD simulations. Our combined approach shows that OH is mainly located at the surface of the liquid and the reaction and the diffusion behaviour are relatively predictable, while the behaviour of H_2O_2 is largely determined by transport effects, which allow for its deep penetration into the liquid.

The comparison of an ideal system, the MD simulations, with a real system, the experiment, can usefully extend the development of a kinetic model. If the molecular diffusion coefficients derived from MD simulations are used directly in kinetic models without consideration of the specific experimental conditions, these models can show large deviations from experimental measurements. This is because, in the experiment, the transportation is never purely diffusion-driven, as it is in the simulations. The use of effective diffusion coefficients derived from experimental measurements indeed leads to good agreement between experimental H_2O_2 transport and kinetic modelling results. However, differences between a kinetic model based on MD data and a model based on experimental data make it possible to separate effects from each other. Experimental transport effects such as diffusion and convection can be better separated from each other by comparing purely diffusion-driven transport from MD simulations. This allows a better consideration of these parts in a kinetic model.

Our results provide valuable insights into the transport processes of reactive species in plasma-treated water, which are essential for optimising plasma-based applications in fields such as medicine and chemical processing. Furthermore, this study underlines the importance of multiscale approaches, to further bridge the gap between theory and experiment. The kinetic model is an effective way to incorporate data from both sources to identify and study the differences between ideal and real conditions, but also gives insights into chemical influence and allows for a high spatial-temporal resolution of the species behaviour. Future studies should focus on exploring the influence of different plasma conditions on the transport and diffusion dynamics to further improve our understanding, as well as the influence of other species delivered from the plasma to the liquid and their interactions inside the liquid.

Data availability statement

The data that support the findings of this study will be openly available following an embargo at the following URL/DOI: https://rdpcidat.rub.de/. Data will be available from 31 March 2025.

Conflict of interest

The authors declare no conflict of interest.

ORCID iDs

Hanna-Friederike Poggemann ⓘ https://orcid.org/0000-0003-4191-6325
Steffen Schüttler ⓘ https://orcid.org/0000-0003-0131-8654
Anna Lena Schöne ⓘ https://orcid.org/0009-0009-6919-7810
Emanuel Jeß ⓘ https://orcid.org/0009-0003-7480-7923
Lars Schücke ⓘ https://orcid.org/0000-0002-7991-853X
Andrew R Gibson ⓘ https://orcid.org/0000-0002-1082-4359
Judith Golda ⓘ https://orcid.org/0000-0003-2344-2146
Christoph Jung ⓘ https://orcid.org/0000-0002-1422-4991

References

[1] Fridman G, Friedman G, Gutsol A, Shekhter A B, Vasilets V N and Fridman A 2008 *Plasma Process. Polym.* **5** 503–33

J. Phys. D: Appl. Phys. **58** (2025) 135208

H-F Poggemann *et al*

[2] Von Woedtke T, Schmidt A, Bekeschus S, Wende K and Weltmann K D 2019 *In Vivo* **33** 1011–26

[3] Bernhardt T, Semmler M L, Schäfer M, Bekeschus S, Emmert S and Boeckmann L 2019 *Oxid. Med. Cell. Longevity* **2019** 1–10

[4] Bogaerts A *et al* 2020 *J. Phys. D: Appl. Phys.* **53** 443001

[5] Bruggeman P J *et al* 2016 *Plasma Sources Sci. Technol.* **25** 053002

[6] Khlyustova A, Labay C, Machala Z, Ginebra M P and Canal C 2019 *Front. Chem. Sci. Eng.* **13** 238–52

[7] Dickenson A, Britun N, Nikiforov A, Leys C, Hasan M I and Walsh J L 2018 *Phys. Chem. Chem. Phys.* **20** 28499–510

[8] Yayci A, Álvaro Gómez B, Krewing M, Fueyo E F, Hollmann F, Alcalde M, Kourist R and Bandow J E 2020 *Chem. Sus. Chem.* **13** 2072–9

[9] Yayci A, Dirks T, Kogelheide F, Alcalde M, Hollmann F, Awakowicz P and Bandow J E 2020 *Chem.Cat. Chem.* **12** 5893–7

[10] Wapshott Stehli H L, Myers B G, Herrera Quesada M J, Grunden A and Stapelmann K 2022 *Plasma Process. Polym.* **19** 2100160

[11] Schüttler S, Schöne A L, Jeß E, Gibson A R and Golda J 2024 *Phys. Chem. Chem. Phys.* **26** 8255–72

[12] Liu D X, Bruggeman P, Iza F, Rong M Z and Kong M G 2010 *Plasma Sources Sci. Technol.* **19** 025018

[13] Gorbanev Y, Verlackt C C W, Tinck S, Tuenter E, Foubert K, Cos P and Bogaerts A 2018 *Phys. Chem. Chem. Phys.* **20** 2797–808

[14] Schröter S *et al* 2018 *Phys. Chem. Chem. Phys.* **20** 24263–86

[15] Van Rens J F M, Schoof J T, Ummelen F C, Van Vugt D C, Bruggeman P J and Van Veldhuizen E M 2014 *IEEE Trans. Plasma Sci.* **42** 2622–3

[16] Hefny M M, Pattyn C, Lukes P and Benedikt J 2016 *J. Phys. D: Appl. Phys.* **49** 404002

[17] Kovačević V V, Sretenović G B, Slikboer E, Guaitella O, Sobota A and Kuraica M M 2018 *J. Phys. D: Appl. Phys.* **51** 065202

[18] Lindsay A, Anderson C, Slikboer E, Shannon S and Graves D 2015 *J. Phys. D: Appl. Phys.* **48** 424007

[19] Verlackt C C W, Van Boxem W and Bogaerts A 2018 *Phys. Chem. Chem. Phys.* **20** 6845–59

[20] Heirman P, Van Boxem W and Bogaerts A 2019 *Phys. Chem. Chem. Phys.* **21** 12881–94

[21] Kamidollayev T and Trelles J P 2023 *J. Phys. D: Appl. Phys.* **0022-3727** 1361–6463

[22] Yusupov M, Neyts E C, Simon P, Berdiyorov G, Snoeckx R, Duin A C V and Bogaerts A 2014 *J. Phys. D: Appl. Phys.* **47** 025205

[23] Duin A C V, Dasgupta S, Lorant F and Goddard W A 2001 *J. Phys. Chem. A* **105** 9396–409

[24] Winzer T, Steuer D, Schüttler S, Blosczyk N, Benedikt J and Golda J 2022 *J. Appl. Phys.* **132** 183301

[25] Schüttler S, Jolmes L, Jeß E, Tschulik K and Golda J 2023 *Plasma Process. Polym.* **21** e2300079

[26] Golda J *et al* 2016 *J. Phys. D: Appl. Phys.* **49** 084003

[27] Golda J, Kogelheide F, Awakowicz P and Gathen V S v d 2019 *Plasma Sources Sci. Technol.* **28** 095023

[28] Urey H C, Dawsey L H and Rice F O 1929 *J. Am. Chem. Soc.* **51** 1371–83

[29] Holt R B, McLane C K and Oldenberg O 1948 *J. Chem. Phys.* **16** 225–9

[30] Oh J S, Szili E J, Gaur N, Hong S H, Furuta H, Short R D and Hatta A 2015 *J. Photopolym. Sci. Technol.* **28** 439–44

[31] Brubaker T R, Ishikawa K, Takeda K, Oh J S, Kondo H, Hashizume H, Tanaka H, Knecht S D, Bilén S G and Hori M 2017 *J. Appl. Phys.* **122** 213301

[32] Oh J S, Szili E J, Ogawa K, Short R D, Ito M, Furuta H and Hatta A 2018 *Jpn. J. Appl. Phys.* **57** 0102B9

[33] Liu Z, Zhou C, Liu D, He T, Guo L, Xu D and Kong M G 2019 *AIP Adv.* **9** 015014

[34] Liberzon A, Lasagna D, Aubert M, Bachant P, Käufer T, Jakirkham Bauer A, Vodenicharski B, Dallas C, Borg J, Tomerast and Ranleu 2020 OpenPIV/openpiv-python: OpenPIV - python (v0.22.2) with a new extended search PIV grid option (available at: https://zenodo.org/record/3930343/)

[35] Adrian R J 2005 *Exp. Fluids* **39** 159–69

[36] Ni Y, Lynch M J, Modic M, Whalley R D and Walsh J L 2016 *J. Phys. D: Appl. Phys.* **49** 355203

[37] Mededovic Thagard S, Stratton G R, Dai F, Bellona C L, Holsen T M, Bohl D G, Paek E and Dickenson E R V 2017 *J. Phys. D: Appl. Phys.* **50** 014003

[38] Lai J, Petrov V and Foster J E 2018 *IEEE Trans. Plasma Sci.* **46** 875–81

[39] Singh B, Rajendran L K, Giarra M, Vlachos P P and Bane S P M 2018 *Exp. Fluids* **59** 179

[40] Morabit Y, Whalley R D, Robert E, Hasan M I and Walsh J L 2020 *Plasma Process. Polym.* **17** 1900217

[41] Park S, Choe W, Lee H, Park J Y, Kim J, Moon S Y and Cvelbar U 2021 *Nature* **592** 49–53

[42] Merényi G, Lind J and Eriksen T E 1990 *J. Biolumin. Chemilumin.* **5** 53–56

[43] Lu C, Song G and Lin J-M 2006 *TRAC Trends Anal. Chem.* **25** 985–95

[44] Merenyi G and Lind J S 1980 *J. Am. Chem. Soc.* **102** 5830–5

[45] Shirai N, Matsuda Y and Sasaki K 2018 *Appl. Phys. Express* **11** 026201

[46] Shirai N, Suga G and Sasaki K 2019 *J. Phys. D: Appl. Phys.* **52** 39LT02

[47] Thompson A P *et al* 2022 *Comput. Phys. Commun.* **271** 108171

[48] Aktulga H M, Fogarty J C, Pandit S A and Grama A Y 2012 *Parallel Comput.* **38** 245–59

[49] Zhang W and Duin A C V 2017 *J. Phys. Chem. B* **121** 6021–32

[50] Monti S, Corozzi A, Fristrup P, Joshi K L, Shin Y K, Oelschlaeger P, Duin A C V and Barone V 2013 *Phys. Chem. Chem. Phys.* **15** 15062–77

[51] Dünweg B and Paul W 1991 *Int. J. Mod. Phys.* C **02** 817–27

[52] Schneider T and Stoll E 1978 *Phys. Rev.* B **17** 1302–22

[53] Brehm M and Kirchner B 2011 *J. Chem. Inf. Model.* **51** 2007–23

[54] Brehm M, Thomas M, Gehrke S and Kirchner B 2020 *J. Chem. Phys.* **152** 164105

[55] Lietz A M and Kushner M J 2016 *J. Phys. D: Appl. Phys.* **49** 425204

[56] Ikuse K and Hamaguchi S 2022 *Jpn. J. Appl. Phys.* **61** 076002

[57] Schröter S, Gibson A R, Kushner M J, Gans T and O'Connell D 2017 *Plasma Phys. Control. Fusion* **60** 014035

[58] Sakiyama Y, Graves D B, Chang H W, Shimizu T and Morfill G E 2012 *J. Phys. D: Appl. Phys.* **45** 425201

[59] Semenov I L, Weltmann K D and Loffhagen D 2019 *J. Phys. D: Appl. Phys.* **52** 315203

[60] The MathWorks Inc 2023 pdepe - Solve 1-D parabolic and elliptic PDEs (available at: https://de.mathworks.com/help/matlab/ref/pdepe.html/) (Accessed 16 January 2025)

[61] Oehmigen K, Hoder T, Wilke C, Brandenburg R, Hahnel M, Weltmann K D and Von Woedtke T 2011 *IEEE Trans. Plasma Sci.* **39** 2646–7

[62] Krynicki K, Green C D and Sawyer D W 1978 *Faraday Discuss. Chem. Soc.* **66** 199–208

[63] Agmon N 1995 *Chem. Phys. Lett.* **244** 456–62

[64] Dong H C, Ho T H, Nguyen T M, Kawazoe Y and Le H M 2021 *J. Comput. Chem.* **42** 1344–53

[65] Zhang W and Duin A C V 2018 *J. Phys. Chem.* B **122** 4083–92